Assessment of the spectral vanishing viscosity LES model for the simulation of coupled molecular radiation and Rayleigh-Bénard convection in a cubic cavity

Maxime Delort-Laval, Laurent Soucasse, Philippe Rivière, Anouar Soufiani

Highlights

Assessment of the spectral vanishing viscosity LES model for the simulation of coupled molecular radiation and Rayleigh-Bénard convection in a cubic cavity

M. Delort-Laval, L. Soucasse, Ph. Rivière, A. Soufiani

- The accuracy of the Spectral Vanishing Viscosity (SVV) LES model is studied in the framework of Rayleigh-Bénard convection.
- Optimal SVV model parameters are determined at $\mathrm{Ra} = 10^9$.
- The model is applied up to $\mathrm{Ra} = 10^{10}$ to study coupled radiation and RB convection in a cubic cavity.
- The most significant effect of radiation is the enhancement of kinetic energy and convective flux.
- Radiation effects are shown to decrease as the Rayleigh number increases from 10^6 to 10^{10}.

Assessment of the spectral vanishing viscosity LES model for the simulation of coupled molecular radiation and Rayleigh-Bénard convection in a cubic cavity

M. Delort-Laval[a], L. Soucasse[a], Ph. Rivière[a], A. Soufiani[a]

[a]*Laboratoire EM2C, CNRS, CentraleSupélec, Université Paris-Saclay, 8-10 rue Joliot Curie, 91192 Gif-sur-Yvette, France*

Abstract

We study the effects of radiative transfer, due to small amounts of water vapor and carbon dioxide in air, on Rayleigh-Bénard flow structure and heat transfer in a cubic cavity up to a Rayleigh number Ra=10^{10}. Direct numerical simulations are carried out, with and without radiative transfer, up to Ra=10^9 and are used to assess the accuracy and to optimize the parameters of a spectral vanishing viscosity (SVV) LES model. Comparisons between SVV and DNS calculations are given in terms of first order and second order statistics, as well as the analysis of spatial auto-correlation functions, and POD eigenmodes. The model is then applied for the highest Rayleigh number Ra=10^{10} considered in this study. Results with and without radiation show a weak influence of radiation on conductive flux, turbulent kinetic energy and variance of temperature fluctuations, while a significant increase of the kinetic energy of the mean flow and of the convective flux are observed when radiative transfer is taken into account. Finally, radiation effects on conductive and convective fluxes, and on the total kinetic energy are analyzed in the Rayleigh number range $10^6 \leq \mathrm{Ra} \leq 10^{10}$. It is shown that these effects decrease when the Rayleigh number increases.

Keywords: turbulent convection, radiative transfer, cubic Rayleigh-Bénard cell, spectral vanishing viscosity model.

Email address: philippe.riviere@centralesupelec.fr (Ph. Rivière)

1. Introduction

Rayleigh-Bénard (RB) convection is a challenging topic for both academic research and for several applications in the field of atmospheric physics, industrial applications, and thermal management of buildings. In several applications involving ambient air, small amounts of water vapor and carbon dioxide are responsible of significant radiative transfer that could affect the mean and fluctuating temperature fields and the resulting thermal convection. The effects of radiation on RB convection, with application to atmospheric physics, have been investigated in the pioneering studies [1, 2, 3]. Using linear stability analyses, radiative transfer was shown to delay the onset of instability due to two mechanisms, namely, the homogenization of the temperature field in the core of the fluid layer (effect on the base state) and the damping of temperature disturbances [4]. Numerical simulations [5, 6] and experimental studies [3] have also confirmed this behavior. However, the above mentioned studies were limited to the first transition to the convection regime or addressed the flow structure and heat transfer just above this transition.

For higher Rayleigh numbers, although several studies have addressed the effects of radiation on natural convection in differentially heated cavities [7, 8, 9, 10], there are very few studies related to radiation effects on RB convection in transitional and turbulent regimes. First attempts have been performed in Refs. [11, 12] for Rayleigh numbers of about $10^6 - 10^7$. However, no full coupling was considered in Ref. [11] and, in Ref. [12], devoted to mixed convection, the gray gas assumption was used for a non-confined thin layer of radiating fluid. A preliminary investigation [13] of radiation effects on RB convection in a cubic cell was limited to $\mathrm{Ra} = 10^7$ and, due to limitations in computational resources, the integration time was not sufficient to capture reorientations of Large Scale Circulation (LSC). More recently, low order models based on Proper Orthogonal Decomposition (POD) have been developed to analyze these LSC reorientations with and without radiation [14, 15] in the range $10^6 \leqslant \mathrm{Ra} \leqslant 10^8$. Similar first eigenmodes were found with and without radiation but with higher energies (eigenvalues) when radiation was taken into account. It was found also that the frequency of reorientation events tends to increase with radiative transfer.

The effects of radiation on heat transfer and flow dynamics inside a cubic cavity were analyzed in Ref. [16] for Rayleigh numbers up to $\mathrm{Ra}=10^9$ with the help of Direct Numerical Simulations (DNS) and a Chebyshev spectral

method. It was found that radiative transfer delays the onset of convection but, once convection settles, it promotes convection and increases the kinetic energy of the flow from Ra $\geq 10^5$. This is a result of the extension of energy exchanges to the core of the cavity while, without radiative transfer, these exchanges are mostly limited to the boundary layers. Gas radiation was shown to increase also all sources of velocity fluctuations and, to a lesser extent, of temperature fluctuations.

To go further and tackle application involving higher Rayleigh numbers, DNS may become impracticable, especially when radiative transfer must be taken into account. It is therefore highly desirable to have approximate but reliable models like the Large Eddy Simulations (LES) that could predict accurately at least the mean flow, heat transfer, and turbulence characteristics. LES consists in resolving the large scales of a fluid flow and modelling the effects of the small scales, mainly the dissipation of the energy. Many models have been proposed since the pioneering study of Smagorinsky [17]. However, these models are not well suited for spectral numerical methods and a different approach has been proposed by Tadmor in 1989, the Spectral Vanishing Viscosity (SVV) model [18, 19]. Spectral methods have the particularity of bringing very few numerical dissipation to the solution, which gives them a very high-order accuracy. However, if not enough modes are used in the spectral representation of the solution, the energy that is transferred to the high modes is not dissipated along the way. The lack of dissipation due to the coarse representation is not compensated by the numerical dissipation and the numerical scheme is unstable.

To avoid this instability, Tadmor introduced a new term in the momentum balance equation designed to add a dissipative component, in order to stabilize the spectral methods. It appears as an operator acting like an hyperviscosity affecting only the high modes of the spectral representation. The ideal form of the operator was discussed in Ref. [20] and took its exponential form with the work in Refs. [21, 22], which has been widely used since then [23, 24].

The aim of the present study is to assess the accuracy of the SVV model in coupled simulations of Rayleigh-Bénard convection with molecular gas radiation in a cubic cavity, and to apply this model at Rayleigh numbers up to Ra=10^{10}. In the presence of gas radiation, it is not possible to define a limited set of dimensionless parameters due to the complex structure of molecular absorption spectra. The cavity size must therefore be prescribed.

In order to make our study relevant for building applications, and to remain consistent with the Boussinesq approximation, the cavity size is extended here to $L = 3$ m while it was set at $L = 1$ m in the previous DNS study [16]. Problem formulation and description of the SVV model are presented in Sec. 2 together with a brief discussion of the employed numerical tools. Comparisons between DNS and SVV results without radiation at Ra=10^8 and Ra=10^9 are used to assess the accuracy and to optimize the parameters of the SVV model in Sec. 3. Model results with optimal parameters are compared in the same section to DNS results, including radiative transfer, at the same value of the Rayleigh number. The model is then applied at Ra=10^{10} and the effects of radiation on the flow field and heat transfer in the range $10^6 \leq \mathrm{Ra} \leq 10^{10}$ are finally discussed in Sec. 4.

2. Problem statement and the SVV model

2.1. Problem set-up

We consider a cubic cavity of size L, heated from the bottom wall and cooled from the top wall, both being considered black (emissivity $\varepsilon = 1$) and isothermal at respective temperatures T_{hot} and T_{cold}. The four side walls are assumed adiabatic and perfectly diffuse reflecting (emissivity $\varepsilon = 0$). The cavity is filled with a radiating air/H_2O/CO_2 gas mixture (see Fig. 1 (a)). In the case of a non-radiating fluid, under the Boussinesq approximation, and neglecting viscous dissipation in energy balance, the problem would be fully controlled by only two dimensionless parameters: the Prandtl number$Pr = \nu_f/a$ and the Rayleigh number $\mathrm{Ra} = g\beta\Delta T L^3/(\nu_f a)$, where ΔT is the temperature difference $\Delta T = T_{\mathrm{hot}} - T_{\mathrm{cold}}$, g is the gravitational acceleration, and where the thermal expansion coefficient β, the kinematic viscosity ν_f and the thermal diffusivity a, are assumed to be uniform. As discussed above (end of Sec. 1), accounting for gas molecular radiation with realistic modelling of radiative properties prevents fully characterizing the problem from only a finite set of dimensionless parameters. In order to make our study relevant for building applications, we consider precisely a radiating air/H_2O/CO_2 gas mixture of molar composition X_{H_2O} =0.02 and X_{CO_2} =0.001, at mean temperature $T_0 = 300$ K and atmospheric pressure, while the cavity size is set to $L = 3$ m. Thermophysical properties, assumed to be uniform (Boussinesq approximation), and not affected by the small amount of water vapor and carbon dioxide, have been evaluated as for pure air at 300 K and atmospheric pressure (thermal conductivity $\lambda = 0.0263$ W

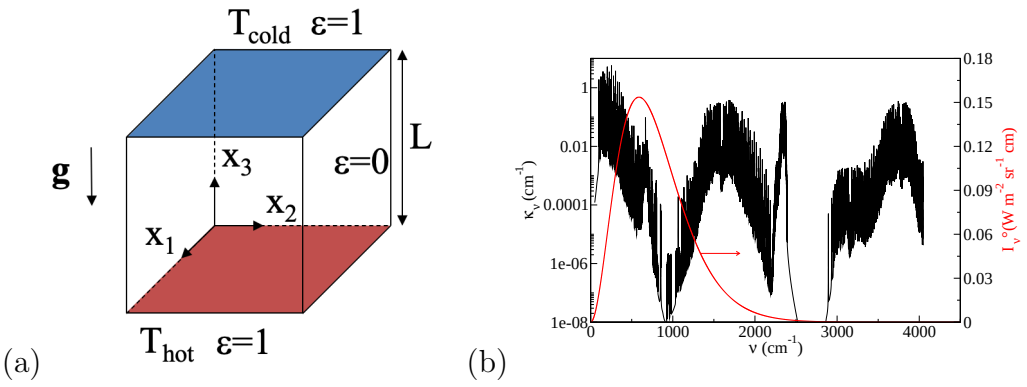

Figure 1: (a) Cubic Rayleigh-Bénard cavity filled with a radiating air/H_2O/CO_2 mixture. Top and bottom walls are isothermal and black while side vertical walls are adiabatic and perfectly diffuse reflecting. (b) Absorption coefficient spectrum of the considered air/H_2O/CO_2 mixture ($T_0 = 300$ K, $X_{H_2O} = 0.02, X_{CO_2} = 0.001$, atmospheric pressure) and Planck function $I^\circ_\nu(T_0)$.

m^{-1} K^{-1}, thermal diffusivity $a = 2.25\times10^{-5}$ m^2 s^{-1}, Prandtl number Pr= 0.707, thermal expansion coefficient $\beta = 1/T_0$). Under these settings, the Rayleigh number is only varied by changing the temperature difference ΔT.

Under the above approximations, the flow is governed according to the following dimensionless mass, momentum, and energy balance equations

$$\frac{\partial u_i}{\partial x_i} = 0, \tag{1}$$

$$\frac{\partial u_i}{\partial t} + u_j\frac{\partial u_i}{\partial x_j} = -\frac{\partial p}{\partial x_i} + \mathrm{Pr}\theta\delta_{i3} + \frac{\mathrm{Pr}}{\sqrt{\mathrm{Ra}}}\frac{\partial^2 u_i}{\partial x_j\partial x_j} + \epsilon_j\frac{\partial}{\partial x_j}\left(Q_j\frac{\partial u_i}{\partial x_j}\right), \tag{2}$$

$$\frac{\partial \theta}{\partial t} + u_j\frac{\partial \theta}{\partial x_j} = \frac{1}{\sqrt{\mathrm{Ra}}}\left(\frac{\partial^2\theta}{\partial x_j\partial x_j} + \mathcal{P}_{\mathrm{rad}}\right) + \epsilon_j\frac{\partial}{\partial x_j}\left(Q_j\frac{\partial\theta}{\partial x_j}\right), \tag{3}$$

where x_j, u_i, p, θ, and $\mathcal{P}_{\mathrm{rad}}$ designate respectively the dimensionless j^{th} Cartesian coordinate, the dimensionless i^{th} velocity vector component, the dimensionless motion pressure, the dimensionless temperature difference $\theta = (T - T_0)/\Delta T$, and the dimensionless radiative source term. Equations (1–3) were made dimensionless using the reference time $L^2/(a\sqrt{\mathrm{Ra}})$, and the reference length L. The additional SVV model terms in the right hand side of Eqs. (2,3) $\epsilon_j\partial_{x_j}(Q_j\partial_{x_j}u_i)$ and $\epsilon_j\partial_{x_j}(Q_j\partial_{x_j}\theta)$ will be discussed in subsection

2.3 and vanish in the reference DNS approach ($\epsilon_j = 0$). The modelling of the radiative source term $\mathcal{P}_{\rm rad}$ is discussed in Sec. 2.4. Equations (1-3) are completed by no-slip boundary conditions on the velocity at the six cavity walls and by the following thermal boundary conditions: $\theta = 0.5/-0.5$ on the horizontal walls $x_3 = 0/1$, and $n_j \partial_{x_j}\theta = 0$ on the four vertical walls $x_1 = 0/1$ and $x_2 = 0/1$, n_j being the coordinates of a wall normal vector. Note that since the vertical adiabatic walls are considered as perfectly reflecting, no radiative coupling term occurs in the energy boundary conditions at these walls where the radiative flux vanishes.

2.2. Numerical methods for the flow field solver

The above flow equations Eqs.(1–3) are solved using a collocation spectral method [25, 26] based on a Chebyshev polynomial expansion for the three directions of space. Time integration is performed through a second-order semi-implicit scheme combining a Backward Differentiation (BDF2) scheme for the linear terms with an Adams-Bashforth extrapolation of the convective terms, while the radiative source term is coupled in an explicit manner as discussed below (§ 2.4). The pressure-flow coupling is ensured by a projection method that forces the velocity divergence free condition. Domain decomposition is applied along the vertical direction to perform parallel computations. A validation of this numerical approach is provided in a previous work [16] for the same Rayleigh-Bénard configuration, in the context of a DNS approach covering a large range of Rayleigh numbers $[10^3 - 10^9]$.

2.3. SVV model

The SVV approach [18, 19] is well suited to reduce the spatial resolution required by an accurate DNS approach in the context of spectral spatial discretization. It consists of compensating for the lack of dissipation resulting from the reduction in spatial discretization by introducing the additional terms in the momentum and energy balance equations $\epsilon_j \partial_{x_j}(Q_j \partial_{x_j} u_i)$ and $\epsilon_j \partial_{x_j}(Q_j \partial_{x_j} \theta)$, where the operators Q_j are defined according to

$$Q_j = \sum_{k_j=0}^{N_j} \widehat{Q}^j_{k_j} P^j_{k_j}. \tag{4}$$

In the above expression, $P^j_{k_j}$ designates the projection operator on $k_j^{\rm th}$ element of the spectral basis (of size $N_j + 1$)(here Chebyshev polynomials T_{k_j},

$k_j = 0, ...N_j$) associated to the j^{th} coordinate, and, when applied to a function $f(x_1, x_2, x_3)$, only acts on the x_j dependence of the function f. The scalars $\widehat{Q}^j_{k_j}$ provide the spectral definition of the operators Q_j; the exponential formulation of Refs. [21, 22] has been retained:

$$\widehat{Q}^j_{k_j} = \begin{cases} 0 & \text{if } k_j \leq M_j, \\ \exp\left(-\frac{(k_j - N_j)^2}{(k_j - M_j)^2}\right) & \text{if } k_j > M_j. \end{cases} \tag{5}$$

Additional SVV terms appear as "artificial" viscosity and thermal diffusivity terms, acting only on the highest modes $k_j > M_j$ of the spectral decomposition: it may be expected that these SVV terms will compensate for the lack of molecular dissipation due to the mesh reduction without introducing large errors on the lowest mode results. Note that the linear form of the SVV additional terms enables a full implicitation in the temporal scheme in a similar manner as for the molecular transport terms, avoiding to penalize the time step choice. Parameters of the model are the weights ϵ_j and the cut-off modes M_j. Optimal choice of these parameters will be examined in Sec. 3.

2.4. Radiative modelling

Under the Boussinesq approximation, the absorption coefficient spectrum κ_ν of the considered radiating air/H_2O/CO_2 gas mixture may be assumed uniform. This high resolution absorption spectrum is shown in Fig. 1 (b) for wave-numbers ν varying between 50 and 4000 cm^{-1}, together with the Planck function at temperature T_0, $I^0_\nu(T_0)$, which enables to calculate the emission spectrum $\kappa_\nu I^0_\nu(T_0)$ according to the Kirchhoff's law. These absorption or emission spectra, containing a few tens of thousands of spectral lines, would require a spectral discretization into about 4×10^5 spectral points to accurately calculate the radiative source term $\mathcal{P}_{\text{rad}}$ directly from a high-spectral description of the gas mixture radiative properties. In order to save computational time, we use the Absorption Distribution Function (ADF) model [27] which consists in substituting the integration over the wavenumber with an integration over the values of the absorption coefficient, for which a coarse logarithmic discretization is sufficient. In the present study, the values of the absorption coefficient of Fig. 1 (b) have been logarithmically discretized in 16 classes and the accuracy of the model has been shown to be better than 1 % [28]. Model parameters and computational details for the considered mixture are given in Refs. [29, 7]. Note that in such a case with uniform

absorption spectrum and gray wall radiative properties, the ADF approach is exact, observed errors only coming from the fineness of the absorption coefficient value discretization.

Using the ADF model, the dimensionless radiative flux at position $\boldsymbol{x} = (x_1, x_2, x_3)$ writes

$$\boldsymbol{q}^{\mathrm{rad}}(\boldsymbol{x}) = \frac{L}{\lambda \Delta T} \sum_k \int_{4\pi} I_k(\boldsymbol{x}, \boldsymbol{\Omega}) \boldsymbol{\Omega} \, d\boldsymbol{\Omega} \tag{6}$$

and the dimensionless radiative power is given by

$$\mathcal{P}_{\mathrm{rad}}(\boldsymbol{x}) = -\boldsymbol{\nabla} \cdot \boldsymbol{q}^{\mathrm{rad}} = \frac{L^2}{\lambda \Delta T} \sum_k \kappa_k \left(\int_{4\pi} I_k(\boldsymbol{x}, \boldsymbol{\Omega}) \, d\boldsymbol{\Omega} - 4 w_k \sigma_{SB} T^4(\boldsymbol{x}) \right), \tag{7}$$

where κ_k and w_k are respectively the absorption coefficient and the weight associated with the k^{th} ADF class and σ_{SB} is the Stefan-Boltzmann constant. The radiative intensity $I_k(\boldsymbol{x}, \boldsymbol{\Omega})$ at position $\boldsymbol{x}$ and direction $\boldsymbol{\Omega}$, associated to the k^{th} ADF class, is obtained by solving the radiative transfer equation for a non scattering medium

$$\boldsymbol{\Omega} \cdot \boldsymbol{\nabla}_{\boldsymbol{x}} I_k(\boldsymbol{x}, \boldsymbol{\Omega}) = \kappa_k \left(\frac{w_k \sigma_{SB} T^4(\boldsymbol{x})}{\pi} - I_k(\boldsymbol{x}, \boldsymbol{\Omega}) \right). \tag{8}$$

The associated boundary condition at wall positions $\boldsymbol{x}^w$ for propagation directions $\boldsymbol{\Omega}$ such that $\boldsymbol{\Omega} \cdot \boldsymbol{n} > 0$, $\boldsymbol{n}$ being the wall normal directed towards the interior of the domain, writes

$$I_k(\boldsymbol{x}^w, \boldsymbol{\Omega}) = \frac{\varepsilon(\boldsymbol{x}^w) w_k \sigma_{SB} T^4(\boldsymbol{x}^w)}{\pi} + \frac{1 - \varepsilon(\boldsymbol{x}^w)}{\pi} \int_{\boldsymbol{\Omega}' \cdot \boldsymbol{n} < 0} I_k(\boldsymbol{x}^w, \boldsymbol{\Omega}') |\boldsymbol{\Omega}' \cdot \boldsymbol{n}| d\boldsymbol{\Omega}'. \tag{9}$$

The radiative transfer equation for each ADF class k Eq. (8) is solved using a ray-tracing algorithm, which was made parallel by distributing the rays among the different processors. The 4π angular domain is uniformly discretized using 900 to 3600 rays from each volume cell center and 450 to 1800 rays from each boundary cell center, depending on the spatial mesh size. The radiation mesh is coarsened by a factor of four to eight in each direction of space compared with the convection mesh and we use a radiation subgrid model [30] to account for the radiation of the spatial scales resolved by the flow mesh but filtered by the coarse radiation mesh. This subgrid model has

been validated in various configurations and its accuracy is approximately a few per cent on radiative power and wall fluxes.

Under the Boussinesq approximation, temperature dependence of gas mixture emission can be linearized; moreover, the gas mixture absorption spectrum is considered as uniform. Thus the radiative source term $\mathcal{P}_{\rm rad}$ appears as a linear function of the temperature field. Therefore, contributions to radiation of spatial scales unresolved by the SVV flow mesh will not contribute to the filtered radiative source term $\mathcal{P}_{\rm rad}$ occurring in the SVV energy balance equation (3), and have been ignored.

Finally, an explicit coupling is carried out between flow and radiation calculations and the radiative power is updated every 5/10 convection time steps δt. Indeed, the flow time step is imposed by numerical stability constraints and does not correspond to significant variations of the temperature field.

3. Optimization and assessment of the SVV model at Ra=10^9

A parametric study is first carried out in this section to analyze the effects of SVV parameters and mesh reduction on the stability and the accuracy of the model. This parametric study is done without radiation at Ra=10^8 and Ra=10^9. Although this sensitivity study was presented in a preliminary publication [31], we reproduce here the main results for the sake of completeness. After the choice of the optimal parameters, comparisons between DNS and SVV results at Ra=10^9 are presented for simulations with and without radiation.

The parametric study consists in testing several values of the cut-off mode and the weight, for different coarsening of the mesh. The number of modes used in the DNS along each direction of space is $N_{\rm DNS} = 160$ at Ra $= 10^8$ and $N_{\rm DNS} = 320$ at Ra $= 10^9$. The number of modes retained in the SVV simulations, N, is characterized by a Mesh Reduction Factor (MRF) according to $N = N_{\rm DNS}/{\rm MRF}$. Three MRF's are studied at Ra $= 10^9$ and two at Ra $= 10^8$. These are summarized in Table 1.

The weight ϵ is usually taken inversely proportional to the number of modes used in the spectral decomposition [19, 20, 21, 32, 23]. The following weights have been considered :

$$\epsilon \in \left\{ \frac{1}{N}, \frac{1}{2N}, \frac{1}{3N}, \frac{1}{4N} \right\}. \tag{10}$$

MRF	1 (DNS)	2	2.67	4
$\mathrm{Ra} = 10^8$	160 (8) [1200]	80 (4) [1200]	60 (3) [1200]	-
$\mathrm{Ra} = 10^9$	320 (16) [400]	160 (8) [400]	120 (6) [400]	80 (4) [400]

Table 1: Number of collocation points N in each direction, for each Rayleigh number and each studied MRF. In parenthesis, the number of domains in the vertical decomposition of the cavity (20 collocation points per domain, in the vertical direction). In brackets, the integration nondimensional time interval for each simulation.

M \ ϵ	$1/N$	$1/2N$	$1/3N$	$1/4N$
$N/2$	$N/2++$	$N/2+$	$N/2-$	$N/2--$
$2N/3$	$2N/3++$	$2N/3+$	$2N/3-$	$2N/3--$
$3N/4$	$3N/4++$	$3N/4+$	$3N/4-$	$3N/4--$
$4N/5$	$4N/5++$	$4N/5+$	$4N/5-$	$4N/5--$

Table 2: Parameters considered for the sensitivity study of the SVV model. In light gray, the configurations investigated in the study and their designations.

As for the cut-off mode, the stability of the SVV model in one-dimensional simulations requires $M \simeq N^\beta$, with $\beta \leq 1/2$ [20] or even $\beta < 1/4$ [19, 18]. But in multidimensional simulations, the condition is not as strict and M is often taken as a fraction of N [20, 21, 32]. The following cut-off modes have thus been considered :

$$M \in \left\{ \frac{N}{2}, \frac{2N}{3}, \frac{3N}{4}, \frac{4N}{5} \right\}. \tag{11}$$

Table 2 summarizes all the 16 combinations of weight and cut-off mode that have to be studied, for the 3 MRF's at $\mathrm{Ra} = 10^9$ and two at $\mathrm{Ra} = 10^8$. To reduce the number of simulations, only half of these combinations were studied : the ones from the diagonal and the anti-diagonal of the table. The spectral representation of the corresponding operator $\epsilon\widehat{Q_k}$ is shown in figure 2 (a).

3.1. Sensitivity of SVV model to the parameters

The combinations of weight and cut-off mode were compared along two criteria: the ability to stabilize the simulation and the ability to accurately predict the basic fluxes in the cavity. Deeper analysis of the accuracy of SVV modeling will concentrate on the optimal set of model parameters and is given in section 3.2.

3.1.1. Stability of the simulations

Figure 2 presents, at $\mathrm{Ra} = 10^9$, the stability of the models for different MRF's. As the mesh gets coarser, it appears that the key parameter for the stability is the cut-off mode M, and the weight ϵ plays almost no role in it. The cut-off mode $M = 4N/5$ seems to be nearly ineffective for stabilizing the simulation: even for MRF = 2, the simulation is not stable for $\epsilon = 1/N$. As the MRF increases, more and more models are unstable and, for MRF = 4, only the models with $M = N/2$ are able to stabilize the simulation. The cut-off mode must therefore be the lowest possible to ensure the stability.

The simulations at $\mathrm{Ra} = 10^8$ were all stable, regardless of the parameters and MRF's studied. This can be explained by the lower level of turbulence than at $\mathrm{Ra} = 10^9$, leading to a smaller amount of kinetic energy that needs to be dissipated at the high-order modes.

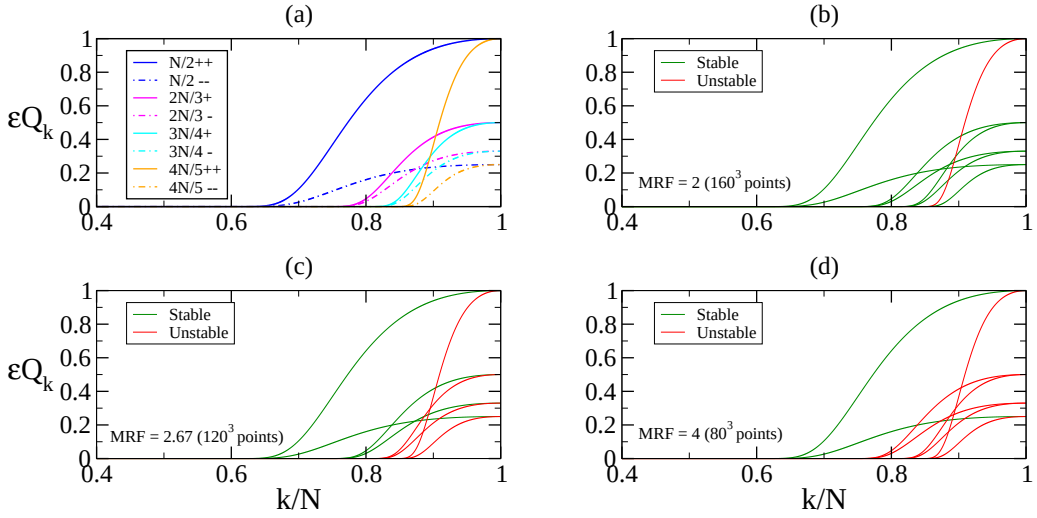

Figure 2: Spectral representation of the studied SVV parameter configurations (a) and the numerical stability for different Mesh Reduction Factors (MRF= N_{DNS}/N) (b), (c) (d). $\mathrm{Ra} = 10^9$.

3.1.2. Prediction of the average heat fluxes

Tables 3 and 4 show, for all the models, Rayleigh numbers and studied MRF's, the conductive flux at the horizontal walls and the convective flux

at the middle plane of the cavity, averaged over time and horizontal plane. Both at $\mathrm{Ra} = 10^8$ and $\mathrm{Ra} = 10^9$, the accuracy of the results decreases as the MRF increases, for every model. For MRF = 2, the SVV model is able to predict accurately both the Nusselt number at the wall and the convective flux in the middle. The accuracy of the model decreases for the lower values of the cut-off mode: this is specially true for $M = N/2$, which gives notably significant differences with the values obtained via DNS.

Here again, the weight seems to have a secondary role compared to the cut-off mode. A high enough cut-off mode ensures good prediction of these basic fluxes, regardless of the weight. It is only when the cut-off mode is too low to guarantee a good accuracy that the weight can play a minor role in correcting the error.

Ra	10^8				10^9					
MRF (Mesh) / Case	2.67 (60)		2 (80)		4 (80)		2.67 (120)		2 (160)	
$N/2++$	33.99	9.4 %	31.54	1.5 %	77.48	25.6 %	68.63	11.3 %	63.14	2.4 %
$N/2--$	33.03	6.3 %	31.28	0.7%	73.85	19.8 %	66.57	7.9 %	62.19	0.8 %
$2N/3+$	32.25	3.8 %	30.97	-0.3 %	-	-	65.1	5.6 %	61.68	0.0 %
$2N/3-$	32.12	3.4 %	30.93	-0.4 %	-	-	64.82	5.1 %	61.41	-0.4 %
$3N/4+$	31.81	2.4 %	30.93	-0.4 %	-	-	-	-	61.34	-0.5 %
$3N/4-$	31.73	2.2 %	30.92	-0.5 %	-	-	-	-	61.33	-0.5 %
$4N/5++$	31.65	1.9 %	30.09	-0.5 %	-	-	-	-	-	-
$4N/5--$	31.44	1.2 %	30.94	-0.4 %	-	-	-	-	61.44	-0.4 %
DNS	31.06				61.67					

Table 3: Mean Nusselt numbers at the top and bottom walls, depending on the Rayleigh number, the MRF and the settings of the SVV model. For each column, the left number is the absolute value of the Nusselt number and the right one is the relative difference with the DNS value. Unstable settings are marked with symbol "-"

3.1.3. Selection of a set of parameters

Of the two parameters of the SVV model, the cut-off mode has the main influence on both the stability and the accuracy. As the MRF increases, the cut-off mode has to be reduced to ensure stability, but the accuracy of the results can be severly downgraded. Therefore, there is no configuration that allows both stability and accuracy for a high MRF. SVV modelling cannot consequently be used with a too coarse mesh and the MRF must be kept around 2.

As a compromise between stability and accuracy, the configuration $2N/3-$ corresponding to $M = 2N/3$ and $\epsilon = 1/3N$ was chosen in the following.

Ra	10^8				10^9					
MRF (Mesh) / Case	2.67 (60)		2 (80)		4 (80)		2.67 (120)		2 (160)	
$N/2++$	34.02	9.6 %	32.22	3.8 %	71.37	15.4 %	67.69	9.4 %	64.44	4.2 %
$N/2--$	32.44	4.5 %	31.62	1.9 %	68.03	10.0 %	66.5	7.5 %	63.08	2.0 %
$2N/3+$	32.8	5.7 %	31.58	1.7 %	-	-	66.44	7.4 %	62.95	1.7 %
$2N/3-$	32.54	4.8 %	31.48	1.4 %	-	-	65.92	6.5 %	62.57	1.1 %
$3N/4+$	31.6	1.8 %	31.26	0.7 %	-	-	-	-	61.95	0.1 %
$3N/4-$	31.74	2.3 %	31.24	0.6 %	-	-	-	-	62.07	0.3 %
$4N/5++$	33.32	7.3 %	31.15	0.4 %	-	-	-	-	-	-
$4N/5--$	32.55	4.9 %	31.15	0.4 %	-	-	-	-	62.01	0.2 %
DNS	31.04				61.87					

Table 4: Mean convective flux at the middle plane of the cavity, depending of the Rayleigh number, the MRF and the settings of the SVV model. For each column, the left number is the absolute value of the convective flux and the right one is the relative difference with the DNS value. Unstable settings are marked with symbol "-".

3.2. Accuracy of the SVV model at Ra=10^9

We present in this section comparisons between DNS and SVV results with the chosen parameters at a Rayleigh number Ra=10^9 for simulations with and without radiation. For the simulations including radiation, the cavity length is $L = 3$ m. The comparisons are given in terms of average vertical profiles of various first and second order moments, then a comparison between Proper Orthogonal Decomposition (POD) modes and spectra is discussed, and, finally, we compare some temperature auto-correlation functions in a plane close to the hot horizontal wall. Simulation parameters, i.e. the number of collocation points and integration time, are those given in Table 1, except for the DNS simulations including radiation where the integration time after statistical convergence was limited to 100 nondimensional time units, due to very important computational cost. The mesh reduction factor was set to $MRF = 2$ for SVV simulations.

3.2.1. Mean vertical profiles

Figures 3 and 4 present, respectively for the cases without radiation and with radiation, vertical profile of key flow quantities averaged temporally and spatially over horizontal planes. These quantities are: the temperature $\overline{\theta}$, the square of temperature fluctuations $\overline{\theta'^2}$ (with a zoom near the hot wall), the conductive flux $-\partial\overline{\theta}/\partial x_3$ (with a zoom), the convective flux $\overline{u_3\theta}$, the kinetic energy of the mean flow $\overline{u}_i\overline{u}_i/2$, and the turbulent kinetic energy $\overline{u'_iu'_i}/2$. For simulations including radiation, the radiative power $\mathcal{P}_{\rm rad} = -\boldsymbol{\nabla}\cdot\boldsymbol{q}^{\rm rad}$ and

the radiative flux $\boldsymbol{q}^{\mathrm{rad}}$ are also displayed.

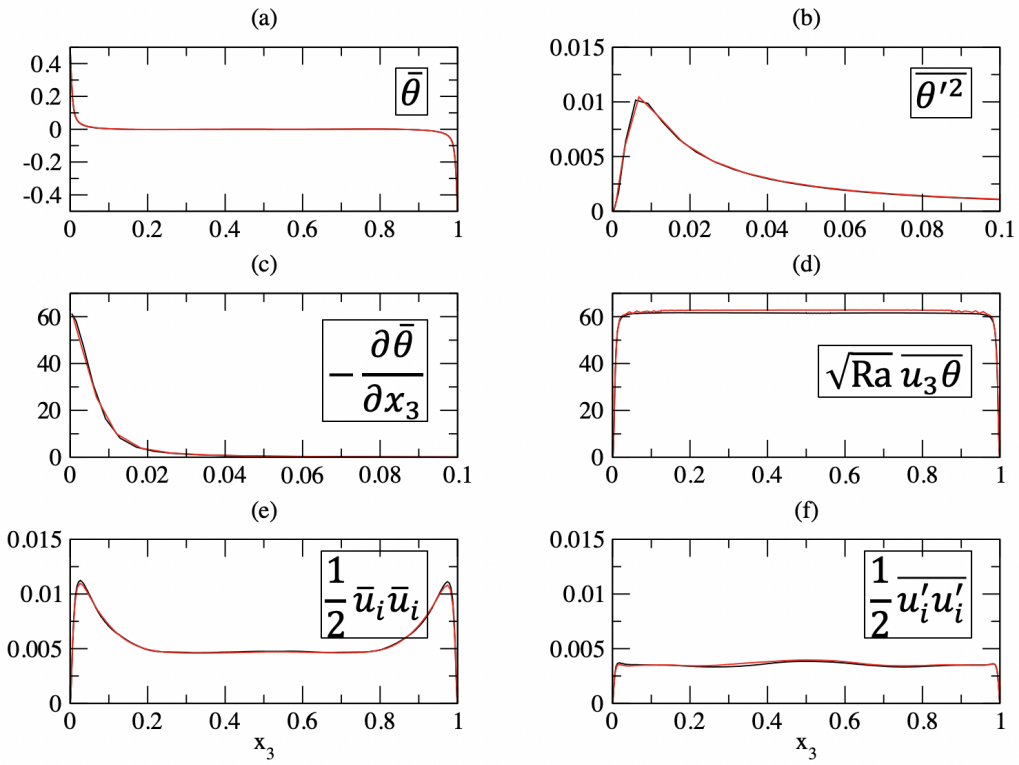

Figure 3: Vertical profiles of key flow parameters averaged over horizontal planes at Ra=10^9 without radiation. DNS results are in black and SVV results in red.

SVV results are shown to be in good agreement with DNS results for all averaged quantities. The most significant differences appear for the convective flux which is overestimated by the SVV model by around 2% at the center of the cavity, and for the turbulent kinetic energy in the case with radiation where differences up to 9.8% are observed. As for radiation, it appears that both radiative fluxes and their divergence are well predicted when using the SVV model, which reinforce the assumption that radiative transfer due to the small scales that are not captured by the radiation subgrid model are negligible in comparison with the effects of modelled scales.
The SVV model appears therefore to be able to predict moments of order one and two with a fair good accuracy.

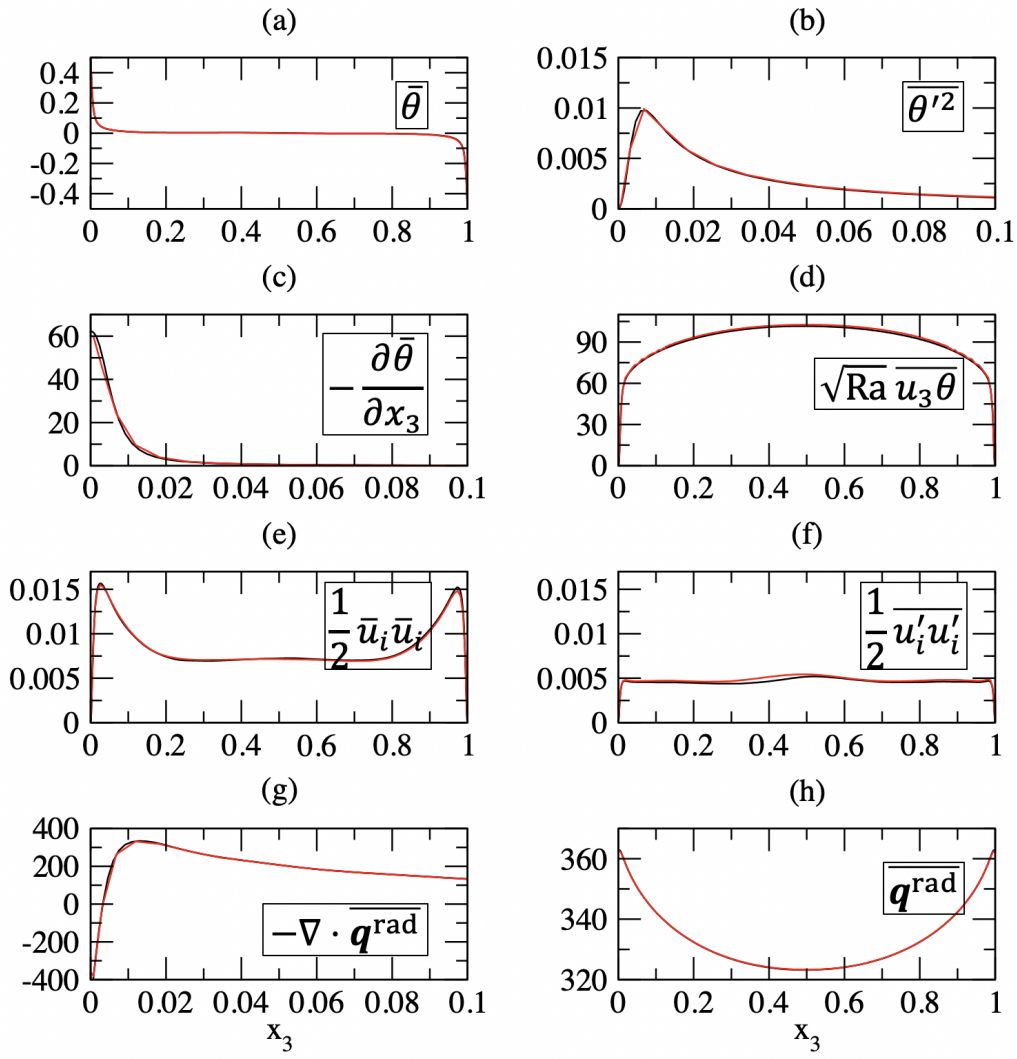

Figure 4: Vertical profiles of key flow parameters averaged over horizontal planes at Ra=10^9 with radiation. DNS results are in black and SVV results in red.

3.2.2. POD analysis

A Proper Orthognal Decomposition (POD) analysis has been carried out to assess the ability of the SVV model to capture the most energetic spatial modes of the flow and temperature fields. Exactly the same procedure as in Ref. [15], based on the snapshot method of Sirovich [33], was employed

to determine the POD eigenmodes and eigenspectrum. 109 snapshots where used in each case (DNS, SVV, with and without radiation) with a fixed sampling period of one dimensionless time unit. In all cases, the analysis of flow angular momenta showed that the Large Scale Circulation (LSC) was organized in vertical diagonal planes and no reorientations were observed. This is probably an artefact owing to the relatively short simulation time compared with the time scale separating two possible reorientations, especially at high Rayleigh number. In order to enforce an equal statistical weight for each flow state and to improve the convergence of the POD method, we have built enlarged snapshot sets, obtained by the action of the 16-elements symmetry group of the problem on the original snapshot sets, as described in [15]. This led to 1744 snapshots for each simulation.
The first 8 POD modes are given in Appendix A together with their description. It is worth noticing that, while the POD analysis given in [15] was limited to Ra=10^8, we retrieve here the same leading modes at Ra=10^9, regardless of whether the simulation is done with DNS or SVV model, with or without radiation. The robustness of the leading modes was also observed in [15] for $10^6 \leq \mathrm{Ra} \leq 10^8$, even if the order of the intermediate modes may change.
Figures 5 and 6 show the eigenspectra obtained from DNS and SVV simulations, without and with radiation, respectively. The energy levels of the first four modes are almost identical, which confirms the ability of the SVV simulations to correctly reproduce the LSC. From the 5th mode (the degenerate modes BL_x and BL_y or L_z), the SVV model tends to slightly overestimate the energy of the intermediate modes, in the case without radiation. In the case with radiation, the energy of the modes is first overestimated, then underestimated. For the highest modes ($n > 15$), the agreement between the DNS and SVV spectra is excellent.
It can be concluded that the SVV model predicts accurately the energy of the leading POD modes, with slight differences for the intermediate modes.

3.2.3. Spatial temperature auto-correlation function

In order to further assess the ability of the SVV model to predict the spatial distribution of turbulent structures in the flow field, we calculated the auto-correlation function in horizontal planes of the temperature field near the bottom wall (non-dimensional distance to the bottom wall $z = 0.007$). The auto-correlation function was calculated using the Wiener-Khinchin theorem, stating that, for a stationary random process, the Fourier spectral de-

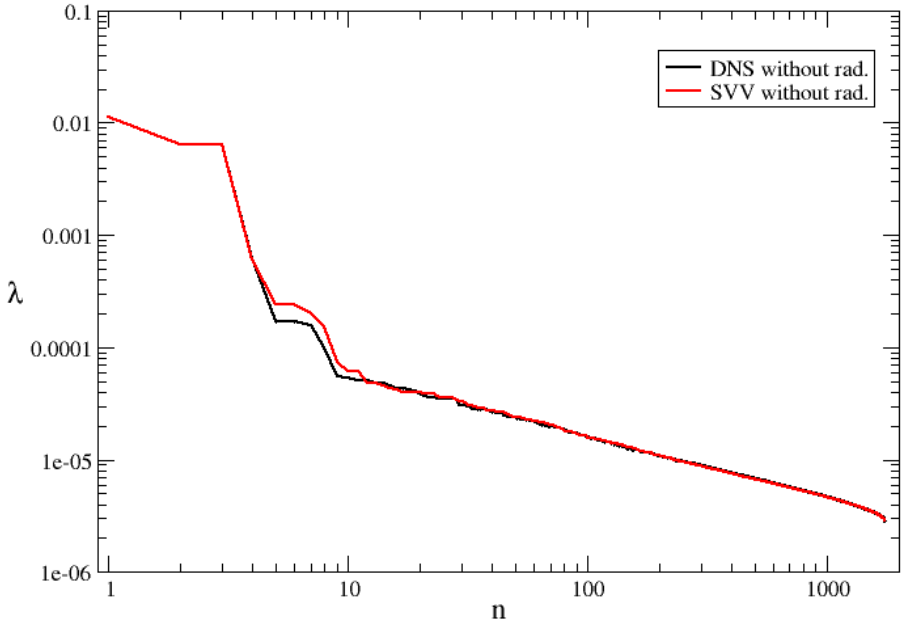

Figure 5: Comparison of POD eigenvalues obtained in the case without radiation from DNS simulations (in black) and SVV simulations (in red) at $\mathrm{Ra} = 10^9$.

composition of the auto-correlation function is equal to the power spectrum of this process.

Let us call $\theta_{z_0}(\boldsymbol{r})$ the two-dimensional temperature field in the plane $z = z_0$, $\widehat{\theta}_{z_0}(\boldsymbol{k})$ its Fourier transform, and $R_{\theta_{z_0}}(\boldsymbol{r}) = \int_\Omega \theta(\boldsymbol{r'})\theta(\boldsymbol{r'}+\boldsymbol{r})d\boldsymbol{r'}$ the auto-correlation function of θ_{z_0}. Then :

$$R_{\theta_{z_0}}(\boldsymbol{r}) = \frac{1}{2\pi}\iint_{-\infty}^{\infty} |\widehat{\theta}_{z_0}(\boldsymbol{k})|^2 \exp(2\imath\pi\boldsymbol{k}\cdot\boldsymbol{r})\, d\boldsymbol{k}. \tag{12}$$

This process is repeated for N_{fields} instantaneous temperature fields and the mean autocorrelation function of the temperature field is then defined by:

$$\overline{R_{\theta_{z_0}}}(\boldsymbol{r}) = \frac{1}{N_{\text{fields}}}\sum_{i=1}^{N_{\text{fields}}} R_{\theta_{z_0},i}(\boldsymbol{r}) \tag{13}$$

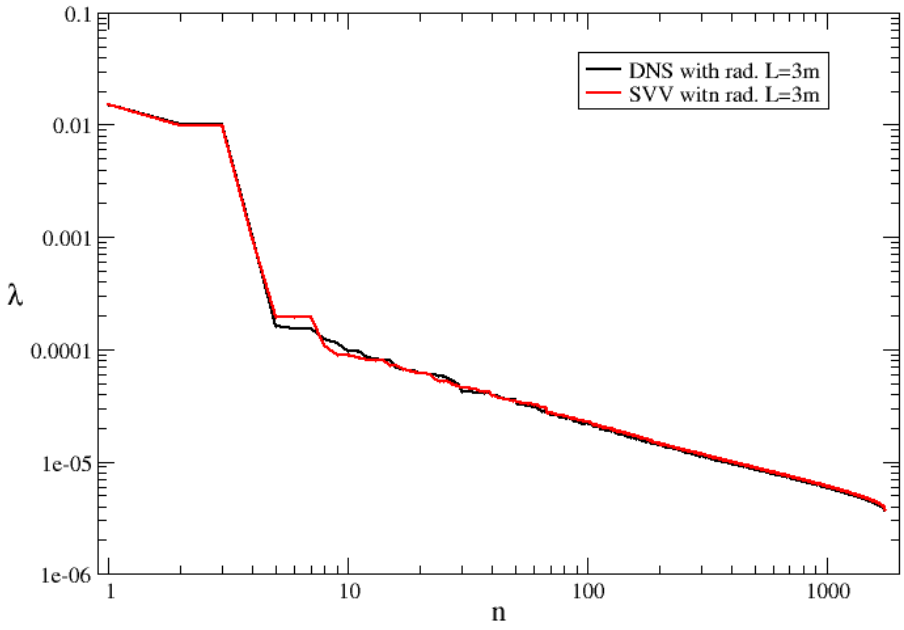

Figure 6: Comparison of POD eigenvalues obtained in the case with radiation from DNS simulations (in black) and SVV simulations (in red) at $\mathrm{Ra} = 10^9$ and $L = 3$ m.

Figure 7 shows examples of instantaneous temperature fields obtained with DNS and with the SVV model, in the case without radiation, as well as the mean autocorrelation functions of the temperature field calculated with $N_{\text{fields}} = 78$ temperature fields, with DNS and SVV simulations.

First, Figures 7 (a) and 7 (b) show similar structures with the signature of a large scale circulation organized around a diagonal plane. To further quantify these structures, the computed averaged auto-correlation functions, shown in Figures 7 (c) for DNS simulations and 7 (d) for the SVV model, are in very good agreement, indicating that the SVV model preserves the length distribution of large scale turbulent eddies and the integral scale of turbulence. The same conclusions may be drawn for simulations including radiative transfer, as shown in Figure 8.

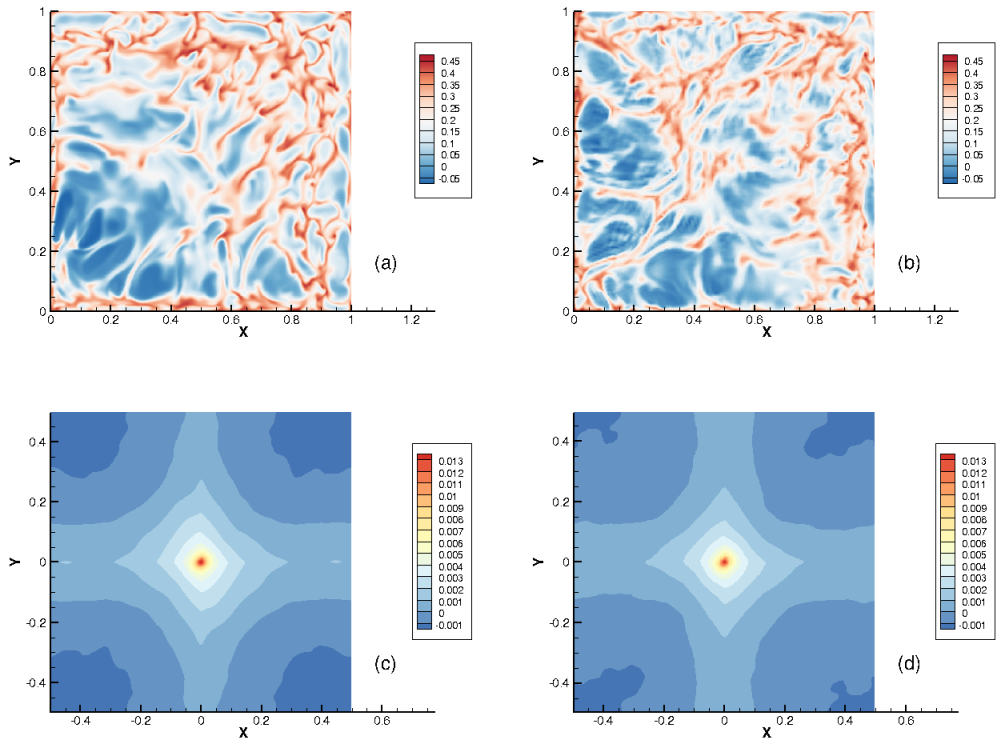

Figure 7: Snapshots of the temperature field at z=0.007 obtained via DNS (a) and SVV, model $2N/3-$ (b) for simulations without radiation. Mean auto-correlation function of the temperature field at z=0.007 for the DNS (c) and SVV (d) simulations, based on 78 snapshots. Ra = 10^9.

4. Radiation effects up to Ra=10^{10}

While comparisons between SVV and DNS results were presented in the previous section, we discuss here the effects of radiative transfer on flow fields and heat transfer. In a first part, radiation effects at Ra = 10^{10} are discussed. Both calculations with and without radiation are carried out using the SVV model. In a second part, radiation effects on global quantities are presented in the range $10^6 \leq$ Ra $\leq 10^{10}$. DNS is employed up to Ra = 10^9 in these comparisons.

The number of collocation points for the calculations at Ra = 10^{10} is 320× 320 × (16×20) points without radiation and 320 × 320 × (16×40)

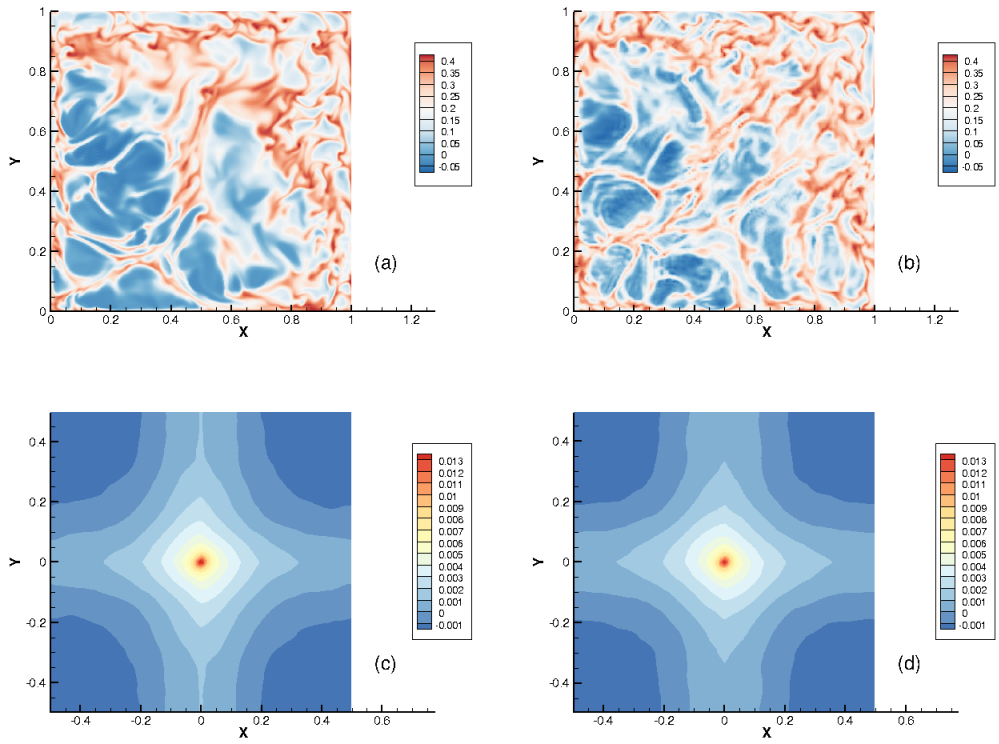

Figure 8: Snapshots of the temperature field at z=0.007 obtained via DNS (a) and SVV, model $2N/3-$ (b) for simulations with radiation (L=3m). Mean auto-correlation function of the temperature field at z=0.007 for the DNS (c) and SVV (d) simulations, based on 78 snapshots. Ra = 10^9

with radiation. As in the previous section, the chosen SVV model is the $2N/3-$ and the integration time, after statistical convergence, was set to 100 nondimensional time units.

Figure 9 shows the vertical distribution of several key quantities averaged over horizontal planes, computed with and without radiation. At this high value of the Rayleigh number, radiation effects are not as important as what was shown in Ref. [16] at smaller Rayleigh numbers. The effects on the mean temperature, temperature fluctuation variance, and on the conductive flux, are nearly invisible. However, a significant increase of the mean kinetic energy and of the convective flux are observed when gas radiation is taken into account. This increase in the kinetic energy at high Rayleigh numbers

was explained in [16] as a result of the additional source term of potential energy due to the action of radiation on the temperature field. It was also shown to become less important as the Rayleigh number increases.

We summarize in Fig. 10 the evolution of the mean Nusselt number averaged on the bottom wall, and of the mean convective flux at mid-height of the cavity. Three configurations are considered in this figure: the transparent gas case, the radiating case with $L = 3$ m, and calculations for the radiating gas with $L = 1$ m. These last calculations were already presented in [16] up to $\mathrm{Ra} = 10^9$ and are included here to discuss the effects of the cavity size when radiation is taken into account. Note that with the thermophysical properties of air at 300 K, and with $L = 1$ m, a Rayleigh number $\mathrm{Ra} = 10^{10}$ would lead to a temperature difference of more than 100 K, which is no more consistent with the Boussinesq approximation. Therefore, the calculations with a radiating gas mixture and $L = 1$ m are limited to $\mathrm{Ra} = 10^9$. Moreover, for the application of building thermal management, the choice of $L = 3$ m is more appropriate.

Figure 10 shows that radiation has nearly no influence on the conductive Nusselt number. Whatever is the radiation configuration, a scaling of the Nusselt number roughly as $\mathrm{Ra}^{2/7}$ is retrieved as in previous studies [34, 35, 36, 37]. For the transparent case, the convective flux also scales as $\mathrm{Ra}^{2/7}$ since there is a balance between conductive and convective fluxes, and the conductive flux is negligible at mid-height of the cavity. However, when gas radiation is considered, radiative transfer affects this balance and we observe a significant increase of the convective flux which scales as $\mathrm{Ra}^{1/4}$ for $L = 1$ m and as $\mathrm{Ra}^{1/5}$ for $L = 3$ m. Let us recall that for the perfectly insulated vertical walls considered here, there is conservation of the total flux (conductive + radiative + convective) with respect to the vertical axis and, as shown in Fig. 9, the radiative flux is smaller at mid-height of the cavity due to screening effects.
Figure 10 shows also that radiation effects decrease as the Rayleigh number increases. This behavior was already analyzed in Ref. [16] and is confirmed here up to $\mathrm{Ra} = 10^{10}$. In the energy balance equation, assuming that the medium is optically thin, the radiative power roughly scales as

$$\frac{1}{\sqrt{\mathrm{Ra}}}\mathcal{P}_{\mathrm{rad}} = \mathcal{O}\left(\frac{1}{\sqrt{\mathrm{Ra}}}\frac{\kappa_P \sigma T_0^3 L^2}{\lambda}\right) \tag{14}$$

where $\kappa_P = \int \kappa_\nu I_\nu^0(T_0) d\nu \times \pi/(\sigma T_0^4)$ is the Planck mean absorption coeffi-

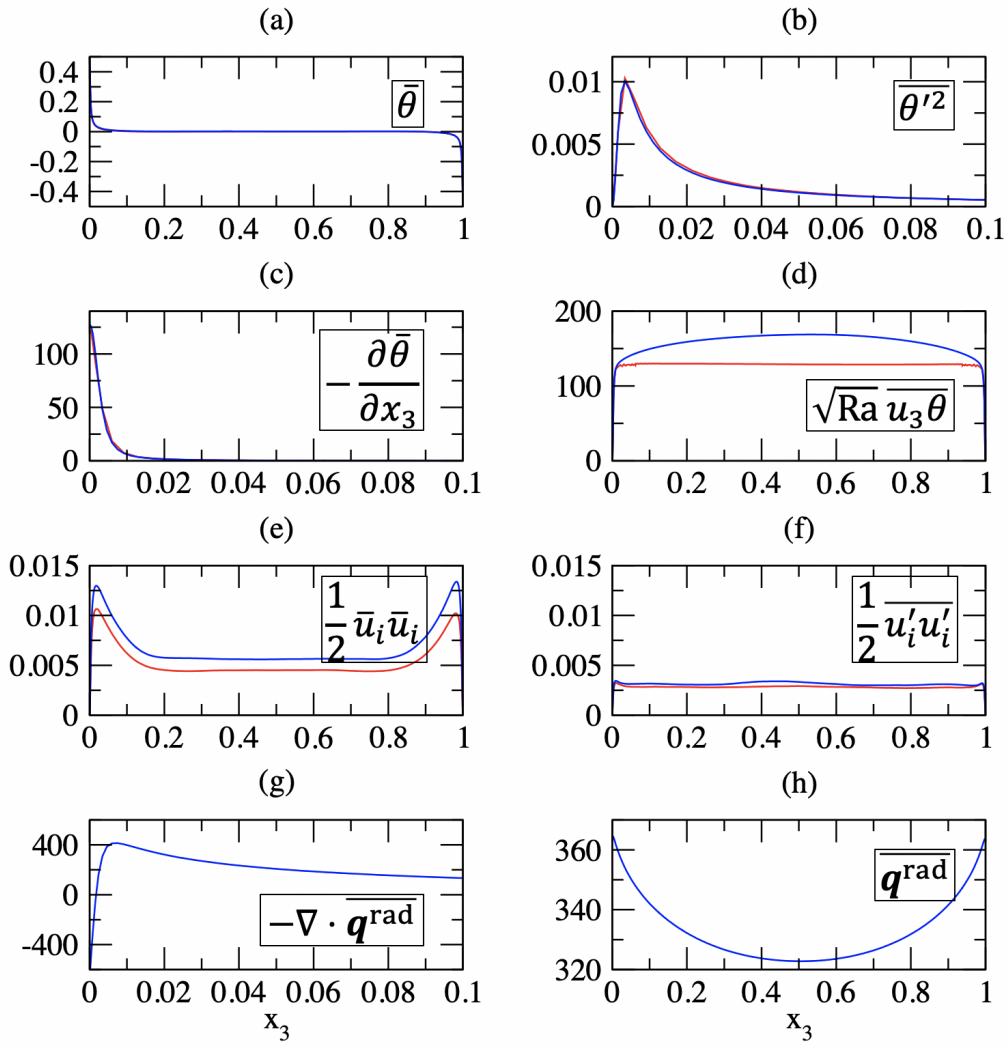

Figure 9: Vertical distribution of key parameters, statistically averaged over time and horizontal planes, at $\mathrm{Ra} = 10^{10}$, for a transparent fluid (red) and a radiating gas mixture with $L = 3$ m (blue). (a) Temperature $\overline{\theta}$, (b) square of temperature fluctuations $\overline{\theta'^2}$ (zoom), (c) conductive flux $-\partial\overline{\theta}/\partial x_3$ (zoom), (d) convective flux $\sqrt{\mathrm{Ra}}\,\overline{u_3\theta}$, (e) kinetic energy of the mean flow $\overline{u}_i\overline{u}_i/2$, (f) turbulent kinetic energy $\overline{u_i'u_i'}/2$, (g) radiative power $\mathcal{P}_{\mathrm{rad}}$, (h) radiative flux $\boldsymbol{q}^{\mathrm{rad}}$.

cient. Thus, the radiative power remains of the same order of magnitude but is penalized by the $1/\sqrt{\mathrm{Ra}}$ factor, whereas the order of magnitude of the

convective term $\boldsymbol{u} \cdot \boldsymbol{\nabla}\theta$ remains the same regardless of the Rayleigh number. Equation 14 also shows that, at a fixed Rayleigh number, the radiative power scales as L^2, which explains the more significant increase of the convective flux in the case $L = 3$ m compared to the case $L = 1$ m. This increase is moreover enhanced by the effects of the actual optical thickness of the medium.

Figure 11 shows the evolution of the total kinetic energy of the flow in the three radiation configurations. In the no-radiation case, the kinetic energy does not vary significantly. This shows that the reference velocity used to make the velocity dimensionless ($u_{ref} = a\sqrt{Ra}/L$), corresponding to a balance between the buoyancy and inertial forces, is well suited for this case. This is no more the case with radiative transfer where the observed significant increase of the total kinetic energy is consistent with the enhancement of the convective flux discussed above.

5. Conclusions

The aim of this study was twofold: assess the accuracy of the spectral vanishing viscosity model, and extend, with this model, previous studies of coupled RB convection and radiation in a cubic cavity up to Ra = 10^{10}. While the SVV model does not have a physical or theoretical basis like other LES models, it makes it possible, through the introduction of an artificial dissipation term of high spectral modes, to ensure the spectral convergence of the numerical scheme.The SVV model depends on the cut-off Chebyshev mode from which the artificial dissipation acts and a weight determining the intensity of the dissipation. Optimal parameters have been determined from a compromise between accuracy and numerical stability in the case of RB convection without radiation in a cubic cavity at a Rayleigh numbers Ra = 10^8 and 10^9. With these optimal parameters, a detailed analysis of model results in cases with and without radiation, through comparisons with DNS results, was carried out at Ra = 10^9. The SVV model was shown to predict velocity and temperature moments of order one and two with a good accuracy. Maximum differences of about 10% were observed however for the turbulent kinetic energy in the radiating case at Ra = 10^9. POD analysis of DNS and SVV results showed that the same most energetic modes are retrieved with the SVV model, even though the order of appearance of some intermediate modes is not always the same. The SVV model was also shown to predict accurately temperature auto-correlation functions, which means

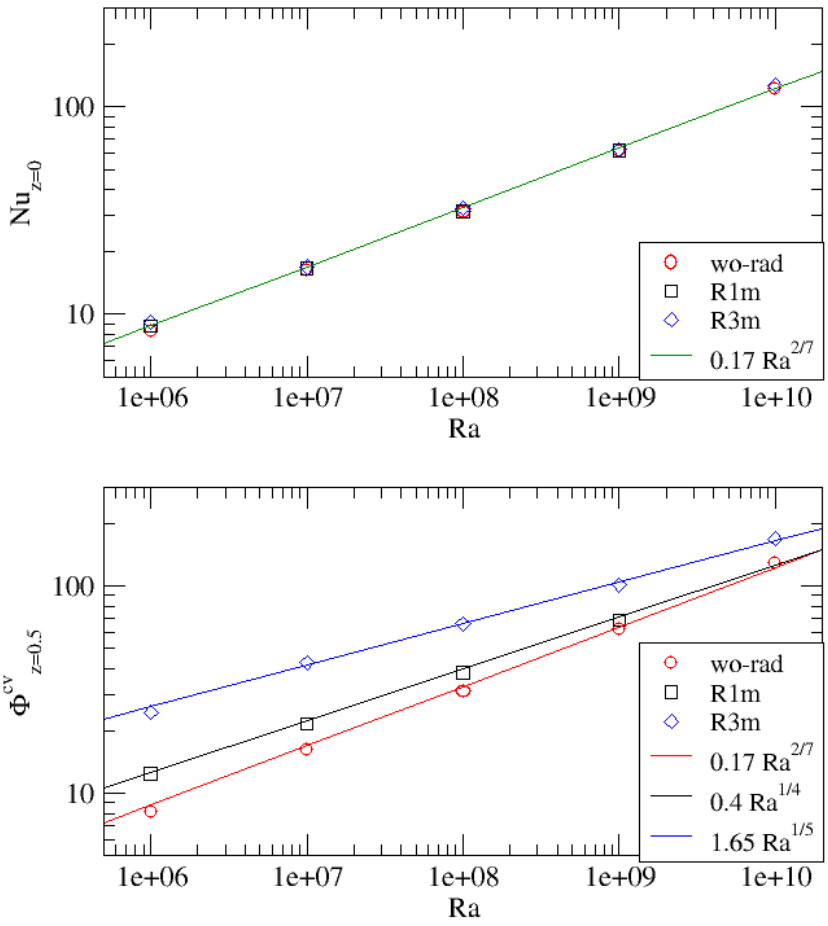

Figure 10: Nusselt number at the bottom wall and the convective flux at mid-height of the cavity as function of the Rayleigh number. Cases without radiation (wo-rad, red), with radiation in a cavity of size $L = 1$ m (R1m, black) and in a cavity of size $L = 3$ m (R3m, blue). Results up to $\mathrm{Ra} = 10^9$ are from DNS simulations.

that the SVV model preserves the length distribution of large scale turbulent eddies and the integral scale of turbulence.

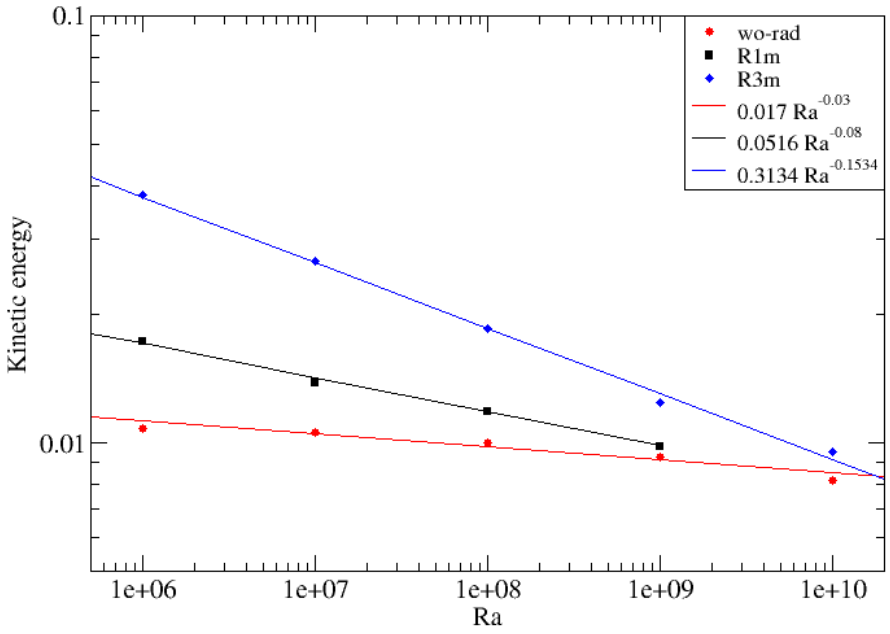

Figure 11: Evolution of the total kinetic energy of the flow with the Rayleigh number. Cases without radiation (wo-rad, red), with radiation in a cavity of size $L = 1$ m (R1m, black) and in a cavity of size $L = 3$ m (R3m, blue). Results up to $\mathrm{Ra} = 10^9$ are from DNS simulations.

The effects of radiative transfer, resulting from small amounts of water vapor and carbon dioxide in ambient air, was studied in the range $10^6 \leq \mathrm{Ra} \leq 10^{10}$. Results from three radiation configurations (no radiation case, radiation in a cavity of size $L = 1$ m, and radiation in a cavity of size $L = 3$ m) were compared in terms of Nusselt number, convective flux at mid-height of the cavity, and total kinetic energy of the flow. It was shown that radiation has nearly no influence on the conductive Nusselt number, but it significantly increases the total circulation in the cavity and then the convective flux and the total kinetic energy. This effect was explained as a result of the action of radiation on the temperature field in the core of the cavity and the resulting increase in potential energy. In accordance with a scaling analysis, these effects of radiation decrease as the Rayleigh number

increases. The same scaling analysis shows that radiative transfer effects increase when the actual size of the cavity increases.

6. Appendix A: POD analysis

We describe in this appendix the eight leading eigenmodes obtained at $\mathrm{Ra} = 10^9$ for the simulations from DNS and SVV models, without and with radiation. They are given respectively in Figures 12 and 13. Two of the modes (L_x and BL_x) are doubly degenerate. With the same notations employed in [15], these modes are:

- Mode M corresponds to the mean flow. It is made of two counter rotating torus.
- The L_x mode correspond to a single large-scale roll around the x axis. It is a doubly degenerate mode with it counterpart L_y (not shown in the figures) which is the image of L_x by a rotation of $\pi/2$ around the vertical axis. When combined, the L_x and L_y modes from a single large-scale diagonal roll.
- The D mode is an 8-roll mode that transports fluid from one corner to the other and strengthens the circulation along the diagonal.
- The BL_x mode is also a doubly degenerate mode (with BL_y, not shown in the figures). It corresponds to two longitudinal corotating structures around the y axis. Modes BL_x and BL_y connect the core of the cell with the horizontal boundary layers.
- The L_z mode is constituted of a single roll lying around the z axis. This is a pure mechanical mode, i.e., its projection on the temperature field is very small.
- The mode C is formed by counter-rotating rolls in the corners of the cavity. It has been shown to play a crucial role in the LSC reorientation phenomena.

These 8 modes are found to be the leading modes in the four simulations (DNS and SVV, with and without radiation). The first four modes appear always in the same order (M, L_x / L_y and D) but, for simulations including radiation, the order of appearance of modes L_z and BL_x / BL_y is inverted between results from DNS and SVV models. However, the energies of these modes are very close as shown in Figure 8.

Aknowledgements

The authors acknowledge the financial support of this study from the French "Agence de l'environnement et de la maîtrise de l'énergie". This work was granted access to the HPC resources of IDRIS under the allocation 2022-A0102B00209 attributed by GENCI (Grand Equipement National de Calcul Intensif). This work was also performed using HPC resources from the Mésocentre computing center of CentraleSupélec and Ecole Normale Supérieure Paris-Saclay supported by CNRS and Région Ile-de-France (http://mesocentre.centralesupelec.fr/).

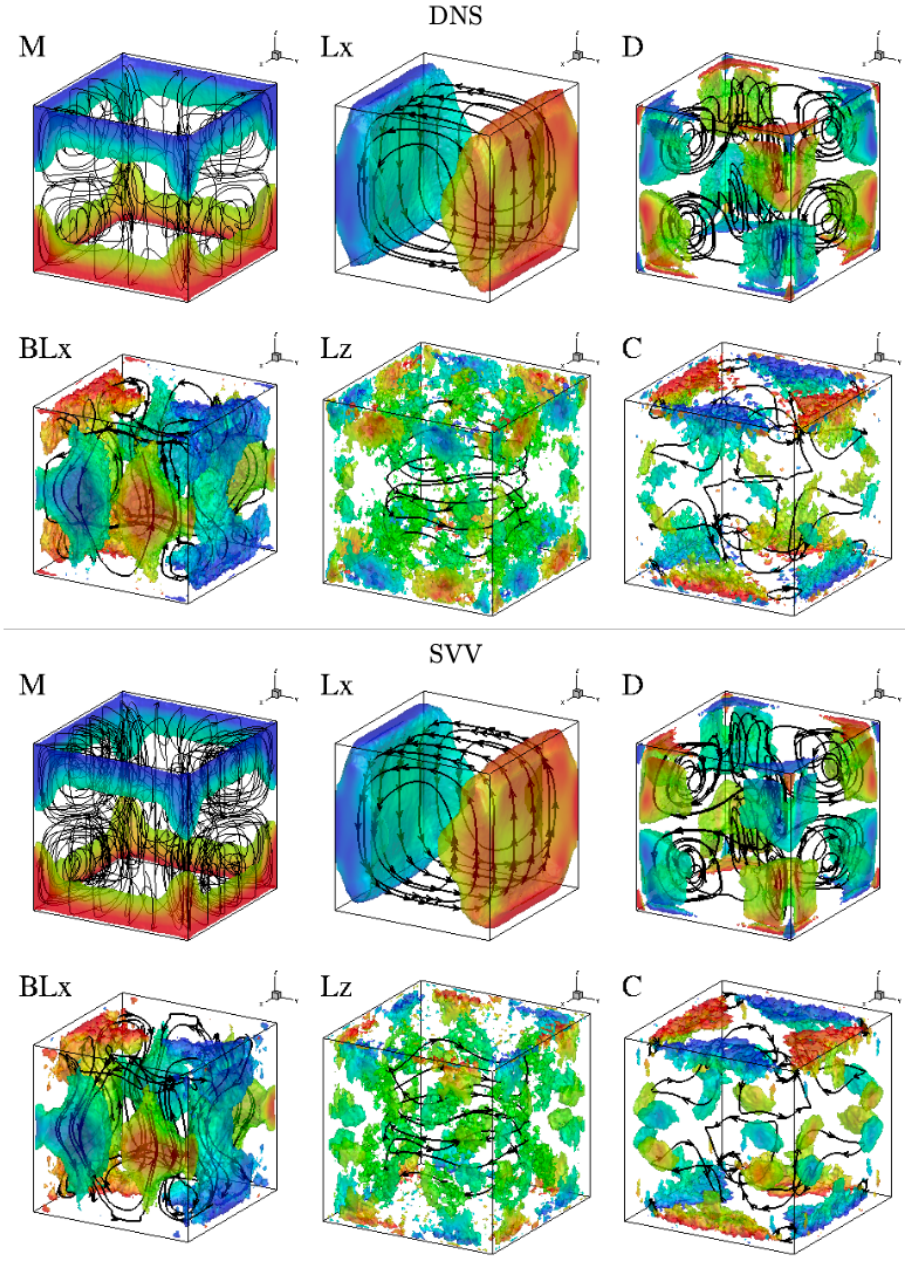

Figure 12: First 8 POD modes obtained in the no-radiation case from DNS simulations (upper graph) and SVV simulations (lower graph). Streamlines and isosurfaces of the contribution to the mean convective heat flux $\phi^w \phi^\theta = 0.1$ (0.01 for mode L_z), colored by mode temperature. For degenerate modes, only the x-oriented one is displayed. Colour map for mode temperature ranges from -0.5 (blue) to 0.5 (red).

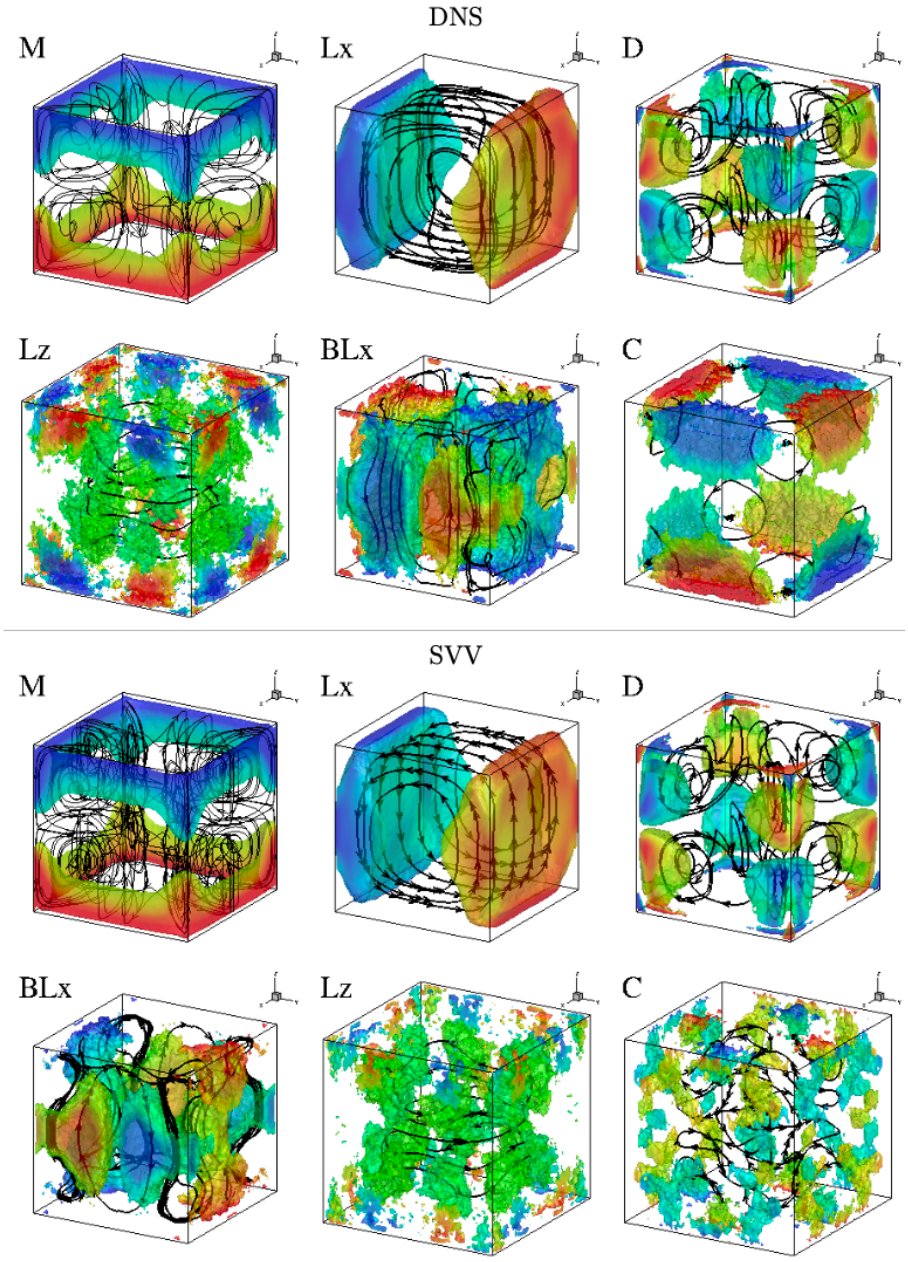

Figure 13: First 8 POD modes obtained in the radiation case with $L = 3$ m from DNS simulations (upper graph) and SVV simulations (lower graph). Streamlines and isosurfaces of the contribution to the mean convective heat flux $\phi^w \phi^\theta = 0.1$ (0.01 for mode L_z), colored by mode temperature. For degenerate modes, only the x-oriented one is displayed. Colour map for mode temperature ranges from -0.5 (blue) to 0.5 (red).

References

[1] E. A. Spiegel, The smoothing of temperature fluctuations by radiative transfer, Astrophysical Journal 126 (1957) 202–207.

[2] E. A. Spiegel, The convective instability of a radiating fluid layer, Astrophysical Journal 132 (1960) 716–728.

[3] J. Gille, R. Goody, Convection in a radiating gas, Journal of Fluid Mechanics 20 (1964) 47–79.

[4] F. Bdéoui, A. Soufiani, The onset of Rayleigh–Bénard instability in molecular radiating gases, Physics of Fluids 9 (1997) 3858–3872.

[5] Bdéoui, F and Soufiani, A, and Le Quéré P., A numerical study of Rayleigh-Bénard convection in radiating gases, in: Proc. of 11th International Heat Transfer Conference, pp. 261-266, Taylor and Francis, 1998.

[6] C. H. Lan, O. A. Ezekoye, J. R. Howell, K. S. Ball, Stability analysis for three-dimensional Rayleigh–Bénard convection with radiatively participating medium using spectral methods, International Journal of Heat and Mass Transfer 46 (2003) 1371–1383.

[7] L. Soucasse, Ph. Rivière, A. Soufiani, S. Xin, P. Le Quéré, Transitional regimes of natural convection in a differentially heated cavity under the effects of wall and molecular gas radiation, Physics of Fluids 26 (2014) 024105.

[8] L. Soucasse, Ph. Rivière, A. Soufiani, Natural convection in a differentially heated cubical cavity under the effects of wall and molecular gas radiation at Rayleigh numbers up to 3×10^9, International Journal of Heat and Fluid Flow 61-B (2016) 510–530.

[9] T. Kogawa, J. Okajima, A. Sakurai, A. Komiya, S. Maruyama, Influence of radiation effect on turbulent natural convection in cubic cavity at normal temperature atmospheric gas, International Journal of Heat and Mass Transfer 104 (2017) 456–466.

[10] T. Kogawa, E. Shoji, J. Okajima, A. Komiya, S. Maruyama, Experimental evaluation of thermal radiation effects on natural convection with a

Rayleigh number of 10^8-10^9 by using an interferometer, International Journal of Heat and Mass Transfer 132 (2019) 1239–1249.

[11] A. Sakurai, R. Kanbayashi, K. Matsubara, S. Maruyama, Radiative heat transfer analysis in a turbulent natural convection obtained from direct numerical simulation, Journal of Thermal Science and Technology 6 (3) (2011) 449–462.

[12] A. Sakurai, K. Matsubara, K. Takakuwa, R. Kanbayashi, Radiation effects on mixed turbulent natural and forced convection in a horizontal channel using direct numerical simulation, International Journal of Heat and Mass Transfer 55 (2012) 2539–2548.

[13] L. Soucasse, Ph. Rivière, A. Soufiani, Effects of molecular gas radiation on Rayleigh-Bénard convection in a 3D cubical cavity, in: Proceedings of the 15th International Heat Transfer Conference, 2014, pp. IHTC15–9563.

[14] L. Soucasse, B. Podvin, Ph. Rivière, A. Soufiani, Reduced-order modelling of radiative transfer effects on Rayleigh-Bénard convection in a cubic cell, Journal of Fluid Mechanics 898 (2020) A2.

[15] L. Soucasse, B. Podvin, Ph. Rivière, A. Soufiani, Low-order models for predicting radiative transfer effects on Rayleigh-Bénard convection in a cubic cell at different Rayleigh numbers, Journal of Fluid Mechanics 917 (2021) A5.

[16] M. Delort-Laval, L. Soucasse, P. Rivière, A. Soufiani, Rayleigh–Bénard convection in a cubic cell under the effects of gas radiation up to Ra=10^9, International Journal of Heat and Mass Transfer 187 (2022) 122453.

[17] J. Smagorinsky, General circulation experiment with the primitive equations, Monthly Weather Review 91 (1963) 99–164.

[18] Y. Maday, E. Tadmor, Analysis of the spectral vanishing viscosity for periodic conservation laws, Siam Journal on Numerical Analysis 26 (1989) 854–870.

[19] E. Tadmor, Convergence of spectral methods for nonlinear conservation laws, Siam Journal on Numerical Analysis 26 (1989) 30–44.

[20] O. Andreassen, I. Lie, C. Wasberg, The spectral viscosity method applied to simulation of waves in a stratified atmosphere, Journal of Computational Physics 110 (1994) 257–273.

[21] G. Karamanos, G. Karniadakis, A spectral vanishing viscosity method for large eddy simulations, Journal of Computational Physics 163 (2000) 22–50.

[22] R. Pasquetti, C. J. Xu, High-order algorithms for large-eddy simulation of incompressible flows, Journal of scientific Computing 17 (2002) 273–284.

[23] M. Minguez, R. Pasquetti, E. Serre, High-order large-eddy simulation of flow over the "ahmed body" car model, Physics of Fluids 20 (2008) 095101.

[24] D. Pitz, J. Chewa, O. Marxen, Effect of an axial throughflow on buoyancy-induced flow in a rotating cavity, International Journal of Heat and Fluid Flow 80 (2019) 108468.

[25] S. Xin, P. Le Quéré, An extended Chebyshev pseudo-spectral benchmark for the 8:1 differentially heated cavity, Numerical Metholds in Fluids 40 (2002) 981–998.

[26] S. Xin, J. Chergui, P. Le Quéré, 3D spectral parallel multi-domain computing for natural convection flows, in: Springer (Ed.), Parallel Computational Fluid Dynamics, Lecture Notes in Computational Science and Engineering book series, Vol. 74, 2008, pp. 163–171.

[27] L. Pierrot, P. Rivière, A. Soufiani, J. Taine, A fictitious-gas-based absorption distribution function global model for radiative transfer in hot gases, Journal of Quantitative Spectroscopy and Radiative Transfer 62 (1999) 609–624.

[28] L. Soucasse, Ph. Rivière, S. Xin, P. Le Quéré, A. Soufiani, Numerical study of coupled molecular gas radiation and natural convection in a differentially heated cubical cavity, Computational Thermal Sciences 4 (2012) 335–350.

[29] L. Soucasse, Effets des transferts radiatifs sur les écoulements de convection naturelle dans une cavité différentiellement chauffée en régimes

transitionnel et faiblement turbulent., Ph.D. thesis, École Centrale Paris, France (2013).
URL https://tel.archives-ouvertes.fr/tel-00978507/document

[30] L. Soucasse, Ph. Rivière, A. Soufiani, Subgrid-scale model for radiative transfer in turbulent participating media, Journal of Computational Physics 257, Part A (2014) 442–459.

[31] M. Delort-Laval, L. Soucasse, P. Rivière, A. Soufiani, Assessment of a spectral vanishing viscosity LES model for 3D Rayleigh-Bénard convection in a cubic cell, in: B. House (Ed.), Proceedings of the 17th International Heat Transfer Conference, IHTC-17 August 14-18, 2023, Cape Town, South Africa, DOI: 10.1615/IHTC17.300-10, 2023.

[32] R. Pasquetti, Spectral Vanishing Viscosity Method for Large-Eddy Simulation of Turbulent Flows, Journal of scientific Computing 27 (2006) 365–375.

[33] L. Sirovich, Turbulence and the dynamic of coherent structures. Part I: Coherent structures, Quarterly of Applied Mathematics 45 (3) (1987) 561–571.

[34] X. Chavanne, F. Chilla, B. Castaing, B. Hebral, B. Chabaud, J. Chaussy, Observation of the ultimate regime in Rayleigh–Bénard convection, Physics Review Letter 79 (1997) 3648–3651.

[35] S. Grossmann, D. Lohse, Scaling in thermal convection: a unifying theory, Journal of Fluid Mechanics 407 (2000) 27–56.

[36] X. Chavanne, F. C. B. Chabaud, , B. Castaing, B. Hebral, Turbulent Rayleigh-Bénard convection in gaseous and liquid he, Physics of Fluids 13(5) (2001) 1300–1320.

[37] G. Ahlers, S. Grossmann, D. Lohse, Heat transfer and large scale dynamics in turbulent rayleigh-bénard convection, Review of Modern Physics 81 (2009) 503–537.